ACS APPLIED MATERIALS & INTERFACES

Research Article

www.acsami.org

Field-Effect Transistors Based on Thermally Treated Electron Beam-Induced Carbonaceous Patterns

Narendra Kurra, Venkata Srinu Bhadram, Chandrabhas Narayana, and G. U. Kulkarni*

Chemistry & Physics of Materials Unit and DST Unit on Nanoscience, Jawaharlal Nehru Centre for Advanced Scientific Research, Jakkur P.O., Bangalore 560 064, India

Supporting Information

ABSTRACT: Electron beam-induced carbonaceous deposition (EBICD) derived from residual hydrocarbons in the vacuum chamber has many fascinating properties. It is known to be chemically complex but robust, structurally amorphous, and electrically insulating. The present study is an attempt to gain more insight into its chemical and electrical nature based on detailed measurements such as Raman, XPS, TEM, and electrical. Interestingly, EBIC patterns are found to be blue fluorescent when excited with UV radiation, a property which owes much to sp^2 carbon clusters amidst sp^3 matrix. Temperature-dependent Raman and electrical measurements have confirmed the graphitization of the EBICD through the decomposition of functional groups above 300 °C. Finally, graphitized EBIC patterns have been employed as active p-type channel material in the field-effect transistors to obtain mobilities in the range of 0.2−4 cm^2/V s.

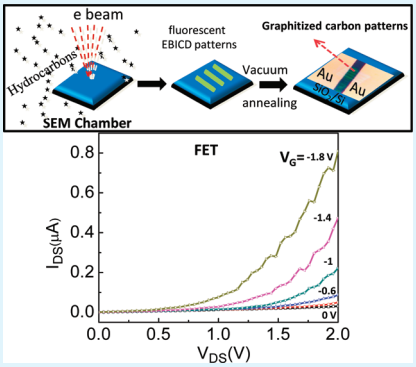

KEYWORDS: *electron beam-induced deposition, amorphous carbon, graphitization, field-effect transistor, field-induced mobility*

1. INTRODUCTION

Carbon is unique, exhibiting a variety of nanoallotropes. Starting from the discovery of the zero dimensional allotrope C_{60}, the saga of carbon nanotubes (1D) and more recently graphene (2D) is astounding. In hindsight, fullerenes and nanotubes may be viewed as single layers of sp^2 graphene rolled in different fashions.[1,2] The way the dimensionality brings about diverse properties in carbon is something unparalleled.[1−4] Although the electrical transport in these materials owes much to the prevalent sp^2 hybridization, an admixture of sp^3 at corners and bends always induces defect levels in a given morphology which often are responsible for the observed interesting properties.[2,5] For instance, C_{60} contains both hexagonal (sp^2 bonding) and pentagonal rings (sp^3 bonding) where the pentagonal rings tend to avoid the delocalization of electrons, making an alkene-like electron deficient system exhibiting semiconducting properties.[6] Carbon nanotubes are considered as bucky tubes with cylindrical morphology, where the properties can be tuned from semiconducting to conducting depending on the tube diameter and chirality.[7] Graphene with lateral dimensions of more than 0.3 μm behaves as a semimetallic system.[8] The edge states of graphene can be metallic or semiconducting depending on the configuration- zigzag or arm chair respectively.[9] The graphene nanoribbons (widths ∼ a few tens of nanometers) show semiconducting properties with opening of a band gap due to edge scattering and quantum confinement.[10] These nanoallotropes find applications in photovoltaics, field effect transistors, sensors and supercapacitors etc.[1−10]

The eldest cousin of these allotropes, the amorphous carbon (a-C), is after all a good mix of sp^2 and sp^3 hybridized carbon atoms, exhibiting both diamond- and graphite-like properties depending on the sp^3/sp^2 ratio, the higher the ratio the better the chemical stability, optical transparency, and mechanical properties.[11−13] Thus, a-C structures have been used as protective coatings for hard discs,[14] and joint implants in the field of medicine.[15] However, the use of a-C material in the electronic devices has been limited due to presence of high density defect states. Graphitization of a-C through thermal treatments may reduce the defect states, making it usable as active material in the functional electronic devices. Recently, Ruan et al. have demonstrated the growth of high-quality graphene on Cu foils starting from natural carbon sources such as food, insects and waste, by thermal treatment in forming gas.[16] Otherwise, carbon deposits in the form of thin films are usually obtained by chemical vapor deposition,[17] pulsed laser deposition,[18] arc discharge methods[19] and sputtering.[20] The above methods involve high temperature and intense plasma conditions where the nature of the carbon produced depends on the deposition conditions and type of the precursor source.[21−23] Although these techniques may offer control on the electrical properties of the carbon deposit, producing patterned carbon deposits with tunable electrical properties at desired locations is still challenging. Here, we employ the direct write technique of electron beam induced carbonaceous

Received: November 28, 2011
Accepted: January 12, 2012
Published: January 12, 2012

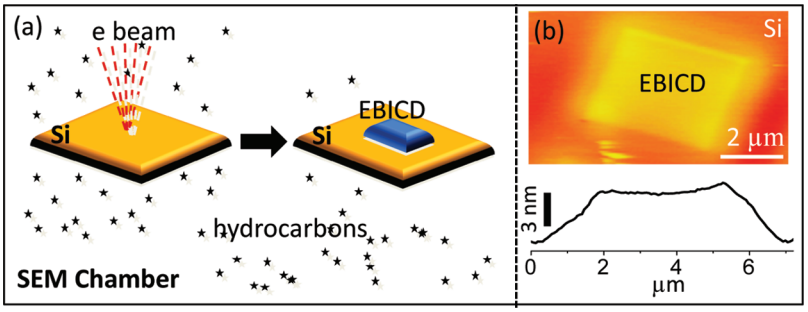

Figure 1. (a) Schematic illustration of the process of electron beam induced carbonaceous deposition (EBICD). (b) AFM topography of the EBICD on Si surface along with the z-profile is shown.

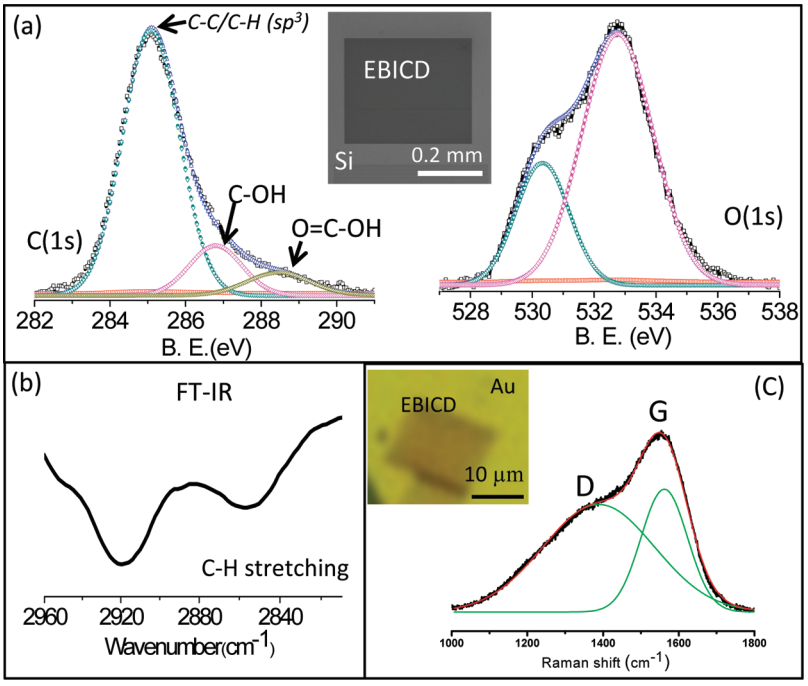

Figure 2. (a) C1s and O1s core-level spectra of the EBICD on Si. The SEM image of the EBIC deposit over large area used for XPS measurement is shown in the inset. Curve fitting of the C1s and O1s spectra was performed assuming a Gaussian peak shape after appropriate background correction. (b) The FT-IR spectrum of EBICD with the presence of C−H stretching vibrational modes. (c) Raman spectra showing the deconvoulted D and G bands of the EBICD. The overlapping D and G bands were deconvoluted by fitting two Gaussian peaks.

deposition (EBICD) to produce patterned regions that have been graphitized by vacuum annealing.

EBICD is usually performed either by supplying the scanning electron microscope (SEM) chamber with a hydrocarbon source such as pump oil[24−26] and paraffin[27] or using residual hydrocarbons[28] present in a low grade vacuum environment. It is chemically robust and electrically insulating in nature. Therefore, it has been employed as an etch resist for micromachining,[29,30] a local dielectric in diode fabrication and CNT circuits,[26,28] and as a glue to lower the electrical contact resistance and strengthen the mechanical characteristics of CNT junctions[31−33] and CNT-AFM tip interfaces.[34−37] Here, in this article, we present a systematic study on the fabrication and electrical characterization of the carbonaceous deposits. Although these findings bring together and augment the literature results,[24−28] we have further investigated the possibility of improving the electrical nature of the patterned deposits by thermal treatment, which for the first time has led to the fabrication of field effect transistors based on EBICD.

2. EXPERIMENTAL SECTION

An n-type Si wafer (ρ = 4−7 Ω cm) was cleaned by sonicating in acetone followed by a rinse in double-distilled water for 2 min. Electron-beam-induced carbonaceous deposition was performed using a field-emission SEM (Nova Nano SEM 600, FEI Company) with a chamber pressure of 1 × 10^{-4} Torr, at a working distance of 3−4 mm. Selected regions on the substrate were exposed to e beam dosages of 0.7−2.5 C cm^{-2} at 10 kV in the patterning mode, large area depositions are made by raster scanning of the e beam in the TV mode. AFM imaging was done on a diInnova SPM (Veeco, USA) using Si probes (model, RTESPA, spring constant 40 N/m) in tapping mode. X-ray photoelectron Spectroscopy (XPS) measurements have been carried out using Omicron SPHERA spectrometer with nonmonochromatic AlKα X-rays (E = 1486.6 eV). Raman spectra of EBICD samples were recorded in the backscattering geometry using a 532 nm excitation from a diode pumped frequency doubled Nd:YAG solid state laser (model GDLM −5015 L, Photop Swutech, China) and a custom-built Raman spectrometer equipped with a SPEX TRIAX 550 monochromator and a liquid nitrogen cooled CCD detector (Spectrum One with CCD3000 controller, ISA Jobin Yvon).Temperature-dependent Raman studies were done using a heating stage (Linkam THMS 600) equipped with a temperature controller

dx.doi.org/10.1021/am201668v | ACS Appl. Mater. Interfaces 2012, 4, 1030−1036

(Linkam TMS 94). The confocal fluorescence images were recorded using a Zeiss LSM 510 laser scanning confocal microscope. For transmission electron microscopy (TEM), the deposition of carbonaceous platforms has been performed on the holey carbon film of the Cu TEM grid. This grid was used for TEM and selected area electron diffraction (SAED) analysis in a JEOL-3010 instrument operating at 300 kV. Vacuum annealed EBIC deposits on the SiO_2/Si surface have been transferred to TEM grid by means of polymethylmethacrylate (PMMA). 50 μL of 3 wt % PMMA ($M_w \approx 996\,000$, Sigma-Aldrich) was drop-coated on the annealed EBIC patterns followed by curing at 150 °C for 2 min. The PMMA film was mechanically peeled off using tweezers. The PMMA film containing EBIC patterns is placed on the TEM grid followed by dissolving the PMMA film after exposing to acetone vapors. The EBIC pattern (thickness ≈ 5 nm) was deposited by irradiation of electron beam (e-dosage 0.7 C cm^{-2} at 10 keV) on a 300 nm SiO_2/Si substrate. This sample was vacuum annealed (pressure =4 x10^{-5} Torr) at a temperature of 500 °C for 30 min to induce graphitization. Finally, 60 nm thick gold source-drain electrodes were deposited (top contacts) by physical vapor deposition (Hind Hivac, Bangalore) through a carbon fiber (diameter, 9 μm) such as P100 as a shadow mask. Transistor measurements were performed using a Keithley 236 multimeter along with a 9 V battery pack for gate voltage.

3. RESULTS AND DISCUSSION

We first examine the chemical nature of the EBICD in some detail and the schematic in Figure 1a illustrates the EBICD process. Our SEM vacuum chamber is pumped by a turbomolecular pump (entire pumping system is designed oil-free at a base pressure of 1×10^{-4} Torr), which is equipped with a nitrogen-purged bearing and is backed by a scroll pump. At this vacuum, water and oxygen exist as residual gases along with possibly little of nitrogen. The hydrocarbon species originate from degassing of the sample holder, conducting glue, etc., enough to cause EBICD under the intense electron beam. E beam seems to induce the cross-linking of hydrocarbon molecules into some polymeric species. This has been well-discussed in the literature.[24−37] The exact chemical reactions leading to EBICD are however, unclear. It is believed that when an electron beam is focused on a substrate, the hydrocarbon molecules in the proximity undergo complex reactions leading to carbonaceous deposition containing sp^3 and sp^2-functionalized carbon.[24−28] The carbonaceous deposition on Si substrate has been performed (see Schematic in Figure 1a) with e dosage of 2.5 C cm^{-2} at 10 kV beam energy. The corresponding AFM image of the EBIC deposit with z-profile showed a nominal thickness of 5 nm with the peripheral regions slightly elevated where the beam returns (see Figure 1b). The thickness of the EBIC deposits can be controlled (from ∼1 to 4 nm as the e dosage increased from 1 to 2.5 C cm^{-2}) depending on the residual pressure in vacuum and e dosage conditions (see Figure S1 in the Supporting Information). Dhaval et. al have also studied the fabrication of EBIC deposits with varying e-dosage conditions.[38]

X-ray photoelectron spectroscopy (XPS) analysis was performed on the EBICD to examine the nature of the carbon present. Figure 2a shows the core level spectra of the EBICD. The C1s spectrum has the main peak at 285.1 eV corresponding to sp^3 C−C and C−H bonding and additional peaks at 286.8 and 288.4 eV assignable to C−OH and O═C−OH species, respectively.[39] The O1s peak positioned at 530.3 eV is assigned to O═C−OH and that at 532.8 eV to C−OH groups. The atomic ratio of carbon to oxygen was estimated to be 3:1 for the EBICD. Since XPS does not clearly distinguish sp^3 C−C and C−H, we have characterized through infrared (IR) analysis. The two vibrational modes at 2920 and 2856 cm^{-1} correspond to the aliphatic C−H stretching modes[40] (see Figure 2b), and this has also been confirmed by the previous studies using various surface spectroscopic studies.[27]

Raman spectroscopy plays an important role in the structural characterization of graphitic materials, especially in providing information about defects, stacking, and finite sizes of crystallites parallel or perpendicular to the hexagonal axis.[41] Performance of the graphitic materials for practical applications is generally influenced by the defects present in these materials. Hence the knowledge of the defects is an important factor in understanding its mechanical and electrical properties. The Raman spectra recorded on the EBICD is shown in Figure 2c. The positions of the D and G bands are centered around 1389 cm^{-1} (fwhm, 274 cm^{-1}) and 1557 cm^{-1} (fwhm, 126 cm^{-1}), respectively (see Figure 2c). In general, the G band relates to the bond stretching vibrations of sp^2 carbon atoms whereas the D band originates from the breathing motion of the 6-fold aromatic rings. The ratio of the intensity of D and G bands (I_D/I_G) is proportional to the probability of finding 6-fold aromatic rings which depends on the sp^2 carbon cluster area in amorphous carbon deposits.[42] The D and G bands being broad, is a clear signature of the amorphous nature of the EBICD (see Figure 2c). Inset shows the EBIC deposits on Au surface. The I_D/I_G ratio was found to be 0.57. It is to be noted that the I_D/I_G ratio is found to be in the range of 0.57−0.88 in the various samples investigated which is common in amorphous carbon (see Figure S2 in the Supporting Information). The emission map is shown in Figure 3

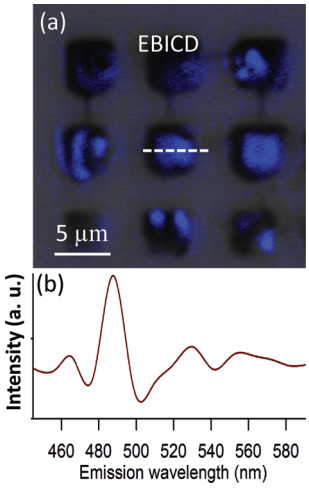

Figure 3. (a) Confocal laser scanning image of the EBIC-deposits; the fluorescence map was obtained by exciting at 355 nm. (b) Emission spectrum of the EBICD with a emission maximum at 485 nm.

(excitation, 355 nm), where the EBIC deposits are seen as blue fluorescent regions and the emission is nonuniform from the EBICD. This weak fluorescent nature arises because of the presence of the carbonyl, carboxyl, and hydroxyl functional groups, which goes well with the XPS analysis. The emission spectrum of the EBICD with a emission maximum at 485 nm is shown in Figure 3b. Based on Raman measurements, the G band arises from the sp^2 carbon domains in the EBICD (see Figure 2c). These sp^2 carbon domains are surrounded by the presence of functional groups which induces localization of electrons giving rise to isolated sp^2 clusters in the sp^3 carbon matrix.[43] These clusters behave as luminescence centers or

chromophores exhibiting fluorescence, originating from the recombination of electron−hole (e−h) pairs, localized within small sp^2 carbon clusters embedded within the functionalized carbon sp^3 matrix.

We have examined the microstructure of the EBICD using TEM. The TEM images of the rectangular shaped carbonaceous platforms on the holey carbon grid are shown in Figure S3a in the Supporting Information. However, it proved difficult to decipher the sp^2 clusters from the rest, due to their small sizes (~1 nm).[43] The electron diffraction patterns from the EBICD are diffused halos, indicating their amorphous nature (see Figure S3b in the Supporting Information).[27]

Raman measurements have shown interesting changes as the EBICD is heated in air at different temperatures (Figure 4). At

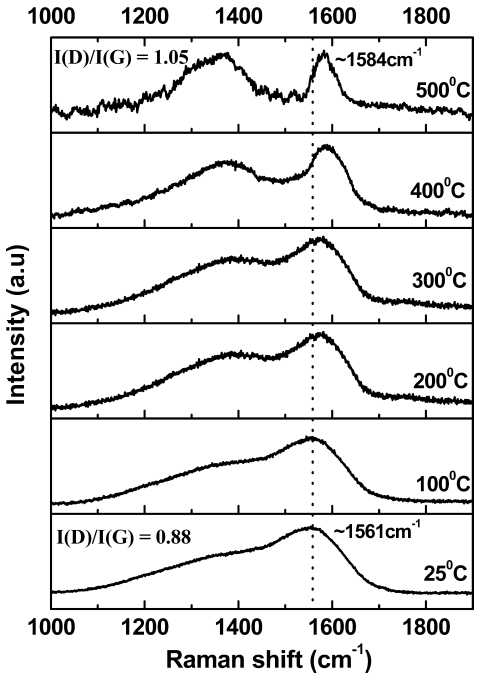

Figure 4. Raman spectra of EBICD recorded at different temperatures in ambient conditions.

room temperature, the D band appears as a shoulder to the G band. As the temperature increases, the fwhm of both D and G bands decrease and peaks become prominent above 300 °C. The G band appearing at 1561 cm^{-1} at room temperature shifts gradually toward higher frequencies as the temperature is increased to position itself finally at 1584 cm^{-1} at 500 °C, similar to the observations of Dillon et al.[44] Defects introduced in the sp^2 carbon network soften the phonon band which, is responsible for broadening of the peaks. The upshift of the G band together with its narrowing of the width indicates that the EBICD becomes progressively defect free (decomposition of functional groups to form nanocrystalline graphite) at higher temperatures.[44] As indicated in Figure 4, I_D/I_G is 0.88 at room temperature, and it increases with temperature to reach 1.05 at 500 °C. The mean crystallite size is estimated to be ~20 nm using the formula[41,42]

$$L_a(\text{nm}) = (2.4 \times 10^{-10})\lambda^4(I_D/I_G)^{-1}$$

A significant increase in the I_D/I_G ratio with temperature indicates that the growth of the sp^2 carbon clusters induce graphitic ordering in the EBICD.[42]

The growth of nanocrystalline graphitic domains with thermal treatment has been further confirmed through AFM and TEM analysis. It is well-known that thermal treatment under ambient conditions, converts the solid EBICD into volatile CO and CO_2 gases. In order to prevent the volatilization, we have annealed the samples under vacuum conditions at 500 °C for 30 min (pressure of 5×10^{-5} Torr). AFM topography shows the presence of nanoparticle domains in the EBICD after vacuum annealing (see Figure 5a). The increase in the roughness of EBICD is due to decomposition of functional groups after the heat treatment (see Figure 1b for the AFM topography of the EBICD). The similar behavior is reflected in the TEM analysis (see Figure 5b). The nanodomains are crystalline in nature as evidenced from the hexagonal electron diffraction pattern from the same region (see inset in the Figure 5b). Therefore, vacuum annealing of the EBICD leading to the formation of nanocrystalline graphitic domains with typical crystallite sizes of 20−30 nm, which is consistent with the Raman studies (Figure 4).

To investigate the electrical nature, we patterned the EBICD on a SiO_2 (300 nm)/Si substrate. Using a shadow mask, a 9 μm gap was produced between the gold contact pads (50 nm thick) deposited on the carbonaceous platform (see Figure S4 in the Supporting Information). The $I-V$ data (Figure 6a) show a blockade region across zero bias (−2 V to +3 V) and beyond −3 V, the curve is slightly asymmetric with current in the range of 20 nA. The $I-V$ behavior of the EBIC deposits (widths of

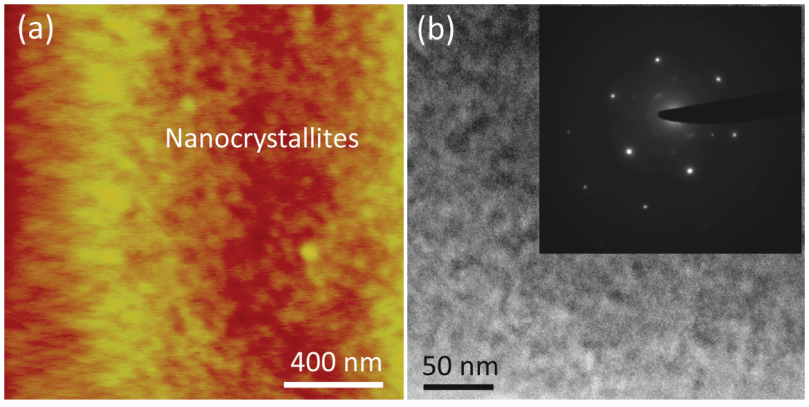

Figure 5. (a) AFM topography and (b) TEM micrograph of the nanocrystalline graphitic domains of the EBICD after vacuum annealing. Inset in b shows the hexagonal electron diffraction pattern from the same region.

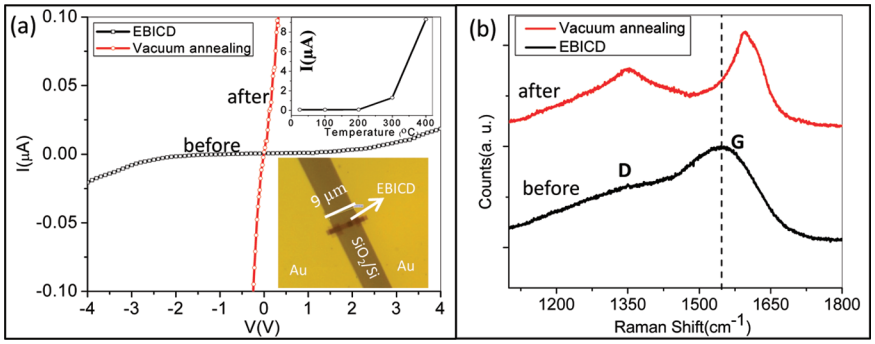

Figure 6. (a) Two probe $I-V$ measurements of the EBICD between two Au electrodes on SiO_2/Si, before (black curve) and after (red curve) vacuum annealing at 500 °C for 30 min. Top inset shows the increase in the conductance of EBICD with temperature under ambient conditions, bottom inset shows the optical micrograph of the EBICD across the gold pads. (b) Raman spectra for the EBICD before (black curve) and after (red curve) vacuum annealing.

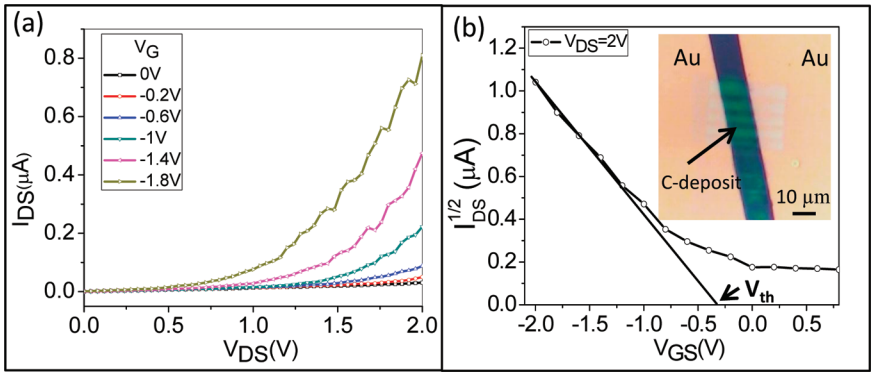

Figure 7. (a) Output and (b) transfer characteristics of thermally annealed carbonaceous patterns on a 300 nm SiO_2/Si substrate with Au source-drain electrodes.

10 and 20 μm across length of 9 μm) between Au contact pads on a glass substrate, confirms the insulating nature (see Figure S5 in the Supporting Information).The EBICD was thermally annealed under vacuum (5×10^{-5} Torr) at 500 °C for 30 min. The $I-V$ data changed significantly (Figure 6a), with current in the range of ~1 μA at a low bias of 1 V, which is at least 3 orders of magnitude higher compared to the pristine deposit.[45] The electrical nature of the EBICD has also been examined under ambient conditions with respect to temperature (see top inset in Figure 6a). The current was monitored with time at a bias of 5 V with increasing temperature. Until 200 °C, there is no change in the current but at 300 °C; current value has increased by an order (0.1 to 1.3 μA). Further enhancement in the current (at least five times) was observed after heating the sample to 400 °C. This can be attributed to the graphitization of EBICD above 300 °C, supporting the temperature dependent Raman studies (Figure 4).[44] The electrical behavior is corroborated by the Raman data. The thickness of the EBICD diminished to a large extent after heating in the ambient conditions because of formation of CO and CO_2 gases. Thermal treatment can decompose the functional groups to induce graphitization in an otherwise insulating EBICD. No major changes were observed after heating the sample for longer times. As discussed in Figure 2c, the EBICD shows broad D and G bands, G band is centered around 1557 cm^{-1} (fwhm, 126 cm^{-1}) (see black curve in Figure 6b). After vacuum annealing, the position of the G band is upshifted to 1599 cm^{-1} and the fwhm decreases to 76 cm^{-1} (see red curve in Figure 6b). This upshift in the G band position and smaller fwhm are clear signatures for the growth of nanocrystalline graphitic domains in the EBICD after vacuum annealing.[42]

We have performed the three terminal electrical transport measurements on vacuum annealed EBICD deposits in the form of stripes between Au source-drain electrodes on SiO_2/Si substrates (Figure 7 and Figures S6 and S7 in the Supporting Information). Figure 7a shows the output characteristics (I_{DS} vs V_{DS}) with varying negative gate voltage (V_G). I_{DS} increases with negative V_G, demonstrating the p-type FET operation, similar to the carbon nanostructures deposited by other methods.[46,47] Four such devices were tried and all exhibited p-type channel behavior with similar low operating voltages. Under ambient conditions due to adsorption of water molecules, electron conduction gets suppressed in carbon materials and the holes become the majority carriers.[48] We have made two devices with top contacts on the thermally treated EBIC-deposits, obtained typical mobilities of 2 and 4 $cm^2/(V\,s)$. On the other hand, the devices with bottom source-drain contacts, showed mobilities below 1 $cm^2/(V\,s)$. The absence of saturation indicates that the conduction is by hopping rather than extended state transport, across the nanocrystalline graphitic domains. The contact resistance at the channel-electrode interface is also responsible for the absence of the saturation currents in the output characteristics similar to the literature reports.[49] On the basis of the transfer characteristics (Figure 7b), the hole mobilities are calculated using the following formula.

$$I_{DS} = (W/2L)C_i\mu(V_G - V_{th})^2 \text{ [for } V_{DS} \geq (V_G - V_{th})\text{]}$$

dx.doi.org/10.1021/am201668v | ACS Appl. Mater. Interfaces 2012, 4, 1030–1036

where I_{DS} = source-drain current; W = width of the channel, 45 μm; L = length of the channel, 9 μm; C_i = capacitance per unit area, 12 nF cm^{-2}; μ = field effect mobility; V_G = gate voltage, −0.4 V. A hole mobility of 4 cm^2/V.s was obtained with V_{th} of −0.3 V and current on−off ratio (I_{on}/I_{off}) of 20. The mobility values of the other three devices came out to be 0.2, 1, and 2 cm^2/(V s). The mobility values are comparable with the nanocrystalline graphene samples fabricated by thermal annealing of self-assembled monolayer and mobility value depends on the annealing temperature.[50] However, crystalline carbon nanomaterials such as carbon nanotubes, graphene and graphene nanoribbons produced by various synthesis methods show very high mobilities (>1000 cm^2/(V s)) but need higher operating voltages for their operation.[51] In our case, because of presence of nanocrystalline domains, the mobilities are low but the devices work at lower operating voltages.

As evident from this study, the simple method of EBICD which enables nanopatterning without the need of an external carbon source can be extended with a following step of vacuum annealing to produce nanocrystalline graphitic domains, which serve as active elements in FET devices. Instead of vacuum annealing, the graphitization of the EBICD can also be achieved by passing higher currents which may decompose the functional groups and induce the graphitization through local joule heating phenomenon. This form of nanocrystalline graphite may also find applications in resistive switching memory where the resistance states can be controlled through the ratio of sp^2/sp^3 carbon bonding through partial graphitization. By introducing suitable organometallic precursors in vacuum during EBICD, the electronic properties of the EBICD can be varied through local doping leads to carbon-based nanoelectronic devices.[52] Another possibility is that EBICD created on catalytic surfaces can possibly be transformed into graphene patterns under suitable annealing conditions. However, there are few limitations, e-beam being a serial patterning technique, limits the throughput. As we rely on residual hydrocarbons present in the vacuum chamber, the nature of the EBICD depends on the quality of the vacuum at that particular time.

3. CONCLUSIONS

The nature of the carbonaceous deposit produced by EBICD is known in the literature. The present study has brought out additional features of the carbonaceous deposit produced by EBICD such as the weak blue fluorescing nature due to presence of functional groups. Following one step vacuum annealing, it has been effectively converted to graphitized carbon patterns which in turn served as an active channel material in field effect transistors. These observations have extended our understanding of both the process and the deposit in terms of its chemical and electrical functionality. The FET devices are of p-type behavior with mobilities in the range of 0.2−4 cm^2/(V s). The operating voltages are rather low (~2 V). We envisage that this form of patterned graphitized EBICD may find applications in all-carbon electronics.[53]

■ ASSOCIATED CONTENT

Supporting Information

The thickness of the carbonaceous deposits with varying e dosage and the Raman spectra of the EBICD on various surfaces (Au, Si, and SiO_2) are presented in Figure S1 and S2. Figure S3 consists of (a) TEM micrograph of the carbonaceous deposits on a holey carbon grid, and (b) the electron diffraction pattern. Figure S4 explains the carbon fiber as shadow mask to deposit contact pads over the EBICD patterns. Two probe I−V of the pristine EBICD on a glass substrate with a width of (a) 10 μm and (b) 20 μm, with a length of 9 μm (Au electrodes) is presented in Figure S5. Figure S6 deals with (a) leakage characteristics of source-gate (SG) and drain-gate (DG) electrodes through 300 nm SiO_2/ Si with 50 nm Au as source-drain electrodes and (b) source-drain leakage characteristics between gold contacts with 9 μm gap. FET action of the thermally annealed carbonaceous deposits with bottom Au contacts is presented in Figure S7. This material is available free of charge via the Internet at http://pubs.acs.org/.

■ AUTHOR INFORMATION

Corresponding Author

*E-mail: kulkarni@jncasr.ac.in. Fax: +91 (80) 22082766. Phone: +91 (80) 22082814.

■ ACKNOWLEDGMENTS

The authors thank Professor C. N. R. Rao, FRS, for his encouragement. Support from the Department of Science and Technology, Government of India, is gratefully acknowledged. NK acknowledges CSIR for funding. The authors thank Veeco India Nanotechnology Laboratory at JNCASR for the AFM facility.

■ REFERENCES

(1) Geim, A. K.; Novoselov, K. S. *Nat. Mater.* **2007**, *6*, 183−191.
(2) Dresselhaus, M. S.; Dresselhaus, G.; Eklund, P. C. *Science of Fullerenes and Carbon Nanotubes*; Academic Press: New York, 1996.
(3) Robertson, J. *Prog. Solid State Chem.* **1991**, *21*, 199−333.
(4) Robertson, J. *Pure Appl. Chem.* **1994**, *66*, 1789−1796.
(5) Wei, D.; Liu, Y. *Adv. Mater.* **2010**, *22*, 3225−3241.
(6) Mintmire, J. W.; Dunlap, B. I.; White, C. T. *Phys. Rev. Lett.* **1992**, *68*, 631−634.
(7) Rao, A. M.; Richter, E.; Bandow, S.; Chase, B.; Eklund, P. C.; Williams, K. A.; Fang, S.; Subbaswamy, K. R.; Menon, M.; Thess, A.; Smalley, R. E.; Dresselhaus, G.; Dresselhaus, M. S. *Science* **1997**, *275*, 187−191.
(8) Novoselov, K. S.; Geim, A. K.; Morozov, S. V.; Jiang, D.; Zhang, Y.; Dubonos, S. V.; Grigorieva, I. V.; Firsov, A. A. *Science* **2004**, *306*, 666−669.
(9) Son, Y.- W.; Cohen, M. L.; Louie, S. G. *Phys. Rev. Lett.* **2006**, *97*, 216803−216806.
(10) Li, X. L.; Wang, X. R.; Zhang, L.; Lee, S. W.; Dai, H. J. *Science* **2008**, *319*, 1229−1232.
(11) Zhang, P.; Tay, B. K.; Sun, C. Q.; Lau, S. P. *J. Vac. Sci. Technol. A* **2002**, *20*, 1390−1394.
(12) Beghi, M. G.; Ferrari, A. C.; Teo, K. B. K; Robertson, J.; Bottani, C. E.; Libassi, A.; Tanner, B. K. *Appl. Phys. Lett.* **2002**, *81*, 3804−3806.
(13) Bull, S. J. *Diamond Relat. Mater.* **1995**, *4*, 827−836.
(14) Petereit, B.; Siemroth, P.; Schneider, H. −H.; Hilgers, H. *Surf. Coat. Technol.* **2003**, *174*, 648−650.
(15) Grill, A. *Diamond Relat. Mater.* **2003**, *12*, 166−170.
(16) Ruan, G.; Sun, Z.; Peng, Z.; Tour, J. M. *ACS Nano* **2011**, *5*, 7601−7607.
(17) Zhang, W.; Catherine, Y. *Surf. Coat. Technol.* **1991**, *47*, 69−83.
(18) Voevdin, A. A.; Donley, M. S. *Surf. Coat. Technol.* **1996**, *82*, 199−213.
(19) Onoprienko, A. A.; Yanchuk, I. B. *Powder Metall. Met. Ceram.* **2006**, *45*, 190−195.
(20) Rother, B.; Siegel, J.; Breuer, K.; Mūhling, I.; Deurschmann, S.; Vetter, J.; Trommer, G.; Rau, B.; Heiser, C. *J. Mater. Res.* **1991**, *6*, 101−111.
(21) Robertson, J. *J. Mater. Sci. Eng., R* **2002**, *37*, 129−281.

(22) Rossi, F.; Andre, B.; Veen, A. V.; Mijnarends, P. E.; Schut, H.; Delplanke, M. P.; Gissler, W.; Haupt, J.; Lucazeau, G.; Abello, L. J. *Appl.Phys.* **1994**, *75*, 3121−3130.
(23) Urso, L. D.; Compagnini, G.; Puglisi, O. *Carbon* **2006**, *44*, 2093−2096.
(24) Koops, H. W. P.; Munro, E.; Rouse, J.; Kretz, J.; Rudolph, M.; Weber, M.; Dahm, G. *Nucl. Instrum. Methods Phys. Res., Sect. A* **1995**, *363*, 1−9.
(25) Schossler, C.; Urban, J.; Kopps, H. W. P. *J. Vac. Sci. Technol. B* **1997**, *15*, 1535−1538.
(26) Miura, N.; Ishii, H.; Shirakashi, J.; Yamada, A.; Konagai, M. *Appl. Surf. Sci.* **1997**, *113*−*114*, 269−273.
(27) Ding, W.; Dikin, D. A.; Chen, X.; Piner, R. D.; Ruoff, R. S.; Zussman, E.; Wang, X.; Li, X. *J. Appl. Phys.* **2005**, *98*, 014905−014911.
(28) Narendra, K; Vijay kumar, T.; Kulkarni, G. U. *J. Nanosci. Nanotechnol.* **2011**, *11*, 1025−1029.
(29) Djenizian, T.; Salhi, B.; Boukherroub, R.; Schmuki, P. *Nanotechnology* **2006**, *17*, 5363−5366.
(30) Morita, N.; Kawasegi, N.; Ooi, K. *Nanotechnology* **2008**, *19*, 155302.
(31) Bachtold, A.; Henny, M.; Terrier, C.; Strunk, C.; Schönenberger, C.; Salvetat, J. P.; Bonard, J. M.; Forró, L. .*Appl. Phys. Lett.* **1998**, *73*, 274−276.
(32) Chen, Q.; Wang, S.; Peng, L. -M. *Nanotechnology* **2006**, *17*, 1087−1098.
(33) Rice, P.; Mitch Wallis, T.; Russek, S. E.; Kabos, P. *Nano Lett.* **2007**, *7*, 1086−1090.
(34) Wang, Y. G.; Wang, T. H.; Lin, X. W.; Dravid, V. P. *Nanotechnology* **2006**, *17*, 6011−6015.
(35) Koops, H. W. P.; Kretz, J.; Rudolph, M.; Weber, M.; Dahm, G.; Lee, K. L. *Jpn. J. Appl. Phys. Part 1* **1994**, *33*, 7099−7107.
(36) Yu, M. −F.; Lourie, O.; Dyer, M. J.; Moloni, K.; Kelly, T. F.; Ruoff, R. S. *Science* **2000**, *287*, 637−640.
(37) Kim, S.; Kim, J.; Berg, M.; de Lozanne, A. *Rev. Sci. Instrum.* **2008**, *79*, 103702−103705.
(38) Kulkarni, D. D.; Rykaczewski, K.; singamaneni, S.; Kim, S.; Fedorov, A. G.; Tsukruk, V. V. *ACS Appl. Mater. Interfaces* **2011**, *3*, 710−720.
(39) Yumitori, S. *J. Mater. Sci.* **2000**, *35*, 139−146.
(40) Subrahmanyam, K. S.; Kumar, P.; Maitra, U.; Govindaraj, A.; Hembram, K. P. S. S.; Waghmare, U. V.; Rao, C. N. R. *Proc. Natl. Acad. Sci. U.S.A.* **2011**, *108*, 2674−2677.
(41) Pimenta, M. A.; Dresselhaus, G.; Dresselhaus, M. S.; Cancado, L. G.; Jorio, A.; Saito, R. *Phys. Chem. Chem. Phys.* **2007**, *9*, 1276−1291.
(42) Ferrari, A. C.; Robertson, J. *Phys. Rev. B.* **2000**, *61*, 14095−14107.
(43) Eda, G.; Lin, Y.-Y.; Mattevi, C.; Yamaguchi, H.; Chen, H.-A.; Chen, I.-S.; Chen, C.-W.; Chhowalla, M. *Adv. Mater.* **2010**, *22*, 505−509.
(44) Dillon, R. O.; Wollam, J. A. *Phys. Rev. B* **1984**, *29*, 3482−3489.
(45) Rykaczewski, K.; Henry, M. R.; Kim, S.-K.; Fedorov, A. G.; Kulkarni, D.; Singamaneni, S.; Tsukruk, V. V. *Nanotechnology* **2010**, *21*, 035202.
(46) Miyajima, Y.; Shkunov, M. S.; Silva, R. P. *Appl. Phys. Lett.* **2009**, *95*, 102102.
(47) Liao, L.; Zheng, M.; Zhang, Z.; Yan, B.; Chang, X.; Ji, G.; Shen, Z.; Wu, T.; Cao, J.; Zhang, J.; Gong, H.; Cao, J.; Yu, T. *Carbon* **2009**, *47*, 1841−1845.
(48) Collins, P. G.; Bradley, K.; Ishigami, M.; Zettl, A. *Science* **2000**, *287*, 1801−1804.
(49) Chabinyc, M. L.; Lu, J.-P.; Street, R. A.; Wu, Y.; Liu, P.; Ong, B. S. *J. Appl. Phys.* **2004**, *96*, 2063.
(50) Turchanin, A.; Weber, D.; Büenfeld, M.; Kisielowski, C.; Fistul, M. V.; Efetov, K. B.; Weimann, T.; Stosch, R.; Mayer, J.; Gölzhäuser, A. *Acs Nano* **2011**, *5*, 3896−3904.
(51) Biswas, C.; Lee, Y. H. *Adv. Funct. Mater.* **2011**, *21*, 3806−3826.
(52) Burghard, M.; Klauk, H.; Kern, K. *Adv. Mater.* **2009**, *21*, 2586−2600.
(53) Avouris, P.; Chen, Z.; Perebeinos, V. *Nat. Nanotechnol.* **2007**, *2*, 605−615.